A special finite element method applied to off-axis tunnel cracking in laminates

Lars P. Mikkelsen [a],*, Brian N. Legarth [b], Leon Herrmann [c], Mikkel M. Christensen [d], Christian F. Niordson [b],*

[a] *Department of Wind Energy, Technical University of Denmark, DK-4000 Roskilde, Denmark*
[b] *Department of Mechanical Engineering, Technical University of Denmark, DK-2800 Kgs. Lyngby, Denmark*
[c] *Chair of Computational Modeling and Simulation, Technical University of Munich, D-80333 Munich, Germany*
[d] *Technical University of Denmark, DK-2800 Kgs. Lyngby, Denmark*

ARTICLE INFO

ABSTRACT

Off-axis oriented tunnel cracking in a laminated structure is modeled using a special 2D off-axis finite element formulation, thus replacing full 3D finite element simulations with much less demanding 2D simulations. The 2D off-axis element is formulated as a user element in the commercial finite element code ABAQUS, and the user element code is made available for the reader. The finite element formulation is used to predict the steady-state energy release rate and the mode-mixity for either one isolated crack or multiple interacting tunnel cracks in the central ply of a $[0/\theta/0/-\theta]_s$ layup. The laminate is loaded uni-axially or bi-axially, and analyses are presented for glass and carbon fiber composites for arbitrary layup angles θ. The 2D finite element model is found to give precise predictions when comparing the detailed simulations made by a full 3D finite element model. It is demonstrated that despite being a 2D method, the model rigorously provides detailed solutions for the out-of-plane deflection and strain. With a speed-up of more than four orders of magnitudes, it is thus possible to perform new, detailed, and very accurate studies of the dependency of laminate thickness as well as neighboring cracks on off-axis tunnel cracking.

1. Introduction

Tunnel cracks are often seen in layered materials where less ductile layers under tensile loading will develop transverse-oriented tunnel cracks when surrounded by more ductile materials, [1,2]. During fatigue loading, tunnel cracks can act as damage initiation points for the subsequently fiber fatigue failure in the load carrying fibers, [3,4]. Hence, understanding and controlling the initiation and growth of such tunnel cracks can potentially have a large influence on the subsequent fatigue damage evolution in the load carrying fibers and therefore on the overall stiffness degradation and fatigue life-time of the laminate.

A large number of studies have addressed 90°, transverse cracks where numerical studies typically rely on 2D plane strain finite element models. In this way, similarly to Beuth [5] for channeling surface cracks, Ho and Suo [6] used an energy balance method based on the crack opening profile of a fully developed tunnel crack and the stress-state of the non-cracked case to obtain steady-state energy release rates. Hutchinson and Suo [7] extended this 2D plane strain analysis to crack interaction studies. Lundmark and Varna [8], used the 2D plane strain model to investigate the stiffness reduction due to the tunnel-crack density while Carraro et al. [9] investigated tunnel-crack-induced delamination. Various other investigations of tunneling cracking at 90° in laminates exist,

such as Cox and Marshall [10] discussing several aspects of the steady-state tunneling cracks, or Crossman et al. [11] and Wang and Crossman [12], treating both tunneling cracks and delamination caused by these cracks. These investigations are typically conducted with generalized plane strain models and thus limited to cracks at 90°.

For orthotropic materials in the presence of weak interfaces, tunnel cracks can develop in other directions than the transverse 90°, direction. An important case is multi-oriented fiber-reinforced polymer plies in composite laminates where the tunnel cracking typically will follow the weak interfaces between the fiber and matrix material. For non-90°, tunnel cracks, the crack-tip will be loaded in a mixed-mode (a combined normal and shear loading). Quaresimin et al. [13] proposed a generalization of the energy balance method for predicting the energy release rate and mode-mixity, which was applied by Maragoni et al. [14] to determine the energy release rate using a 3D finite element model. A prediction based on a full 3D model. Mikkelsen et al. [15] found that the method was giving accurate predictions of both the energy release rate and the mode-mixity even when based on a 3D finite element analysis of a fully developed crack without explicitly modeling the crack-tip stress-field. The numerical solutions showed that the far-field self-similar solutions (far behind the crack front) could be used to determine the crack-tip load based on an energy balance, thus essentially utilizing 2D features of the solution which may be directly modeled using specialized off-axis 2D finite elements.

In the present study, such an off-axis finite element is developed and implemented in the commercial finite element code ABAQUS. The element is used for predicting the energy release rate and mode-mixity for a specific symmetric laminate layup $[0/\theta/0/-\theta]_s$ with a central tunnel-crack in the symmetry ply. The material is assumed to be a linear elastic orthotropic material representing typical glass and carbon fiber composites. Even though only such specific cases are considered, the off-axis finite element framework is relevant for modeling a wide class of problems, including material non-linearity in the form of plasticity as well as micro-mechanical effects such as inhomogeneous stress states between the reinforcing fibers, and effects of curing induced residual stresses — all potentially in combination with crack growth simulations based on 2D energy balances.

The new 2D element formulation has been validated against full 3D simulations by comparison of both the 3D stress-state in a symmetric laminate, the energy release rate and the mode-mixity for tunnel-cracking under uniaxial loading, [15], as well as under bi-axial loading, [16]. The user element can be downloaded from Mikkelsen et al. [17].

2. Tunnel crack model

Fig. 1 shows two different 3D models which can be used for calculating the average steady-state energy release rate, $\bar{G}_{ss}$, and the average mode-mixity, $\bar{\psi}$, for a tunnel crack front positioned in the central layer of the composite layup $[0/\theta/0/-\theta]_s$. Thus, except for the ply thickness studies presented in Fig. 9, the middle layer has the thickness $2h$ whereas all other layers have the thickness h with a resulting total laminate thickness $2H = 8h$. All laminates considered, are then symmetric and balanced. A Cartesian coordinate system, x_i, is aligned with the sides of the laminate. The laminate shown in Fig. 1 is to be loaded in uni-axial tension in the x_1-direction by the average membrane stress N_1, but bi-axial loading with N_3 in the x_3 will also be investigated. The crack front is loaded in mixed Mode I and Mode II. A standard material coordinate system aligned with material directions is also introduced as $(x_L, x_T, x_{T'})$. Here, $x_{T'}$ will always be parallel to x_2 and the angle between x_1 and x_L is θ.

Fig. 1a shows the full cracked laminate. The tunnel crack front in the middle layer is positioned at an arbitrary position in between but far from the laminate edges. The crack front shape will generally vary with x_2, but under steady-state conditions, the average steady-state energy release rate, $\bar{G}_{ss}$, along the crack front can be found as the average value of the J-integral

$$\bar{G}_{ss} = \frac{1}{2h} \int_{-h}^{h} J(x_2) dx_2, \tag{1}$$

and the corresponding average mode-mixity, $\bar{\psi}$, can be defined as

$$\bar{\psi} = \frac{1}{2h} \int_{-h}^{h} \psi(x_2) dx_2 \quad ; \quad \psi(x_2) = \arctan\left(\frac{K_{II}(x_2)}{K_I(x_2)}\right). \tag{2}$$

Here, $K_I(x_2)$ and $K_{II}(x_2)$ are the Mode I and Mode II stress intensity factors, respectively. It is noted that $K_I(x_2)$ and $K_{II}(x_2)$ as well as the J-integral will depend on x_2 in general.

As the layup considered is symmetric and balanced, only half of it needs to be analyzed. Furthermore, in Mikkelsen et al. [15], it was validated by 3D analyses, that the average steady-state energy release rate, $\bar{G}_{ss}$, and the average mode-mixity, $\bar{\psi}$, along the crack front can be found from an off-axis generalization (see [13]) of the energy balancing method described in Beuth [5] and Ho and Suo [6]. Hence, the crack front itself does not need to be represented in the model in order to evaluate the average energy release rate, $\bar{G}_{ss}$, and mode-mixity, $\bar{\psi}$. This is illustrated in Fig. 1b where a full-width crack without any crack front is shown for the half-thickness laminate. Then the average energy release rate, $\bar{G}_{ss}$, and mode-mixity, $\bar{\psi}$, will be taken as a Mode I and a Mode II contribution
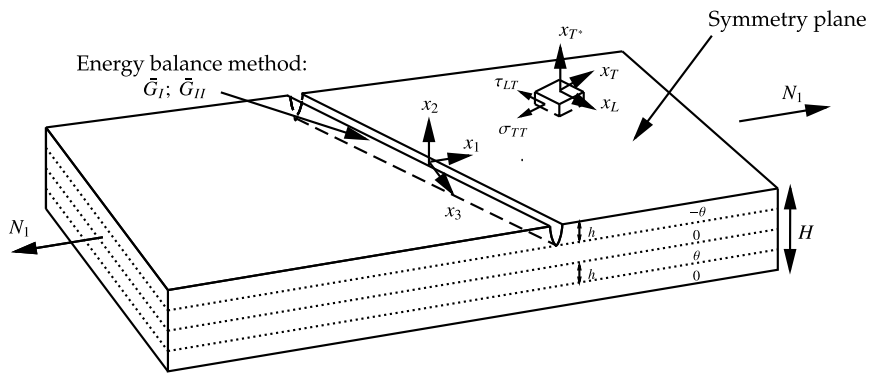
$$\bar{G}_{ss} = \bar{G}_I + \bar{G}_{II} \quad ; \qquad \bar{\psi} = \arctan\left(\lambda^{-1/4} \sqrt{\frac{\bar{G}_{II}}{\bar{G}_I}}\right) \tag{3}$$

with [18]

$$\left\{ \begin{array}{c} \bar{G}_I \\ \bar{G}_{II} \end{array} \right\} = \sqrt{\frac{1+\rho}{2 E_L E_T}} \left\{ \begin{array}{c} \lambda^{-1/4} \bar{K}_I^2 \\ \lambda^{1/4} \bar{K}_{II}^2 \end{array} \right\} \tag{4}$$
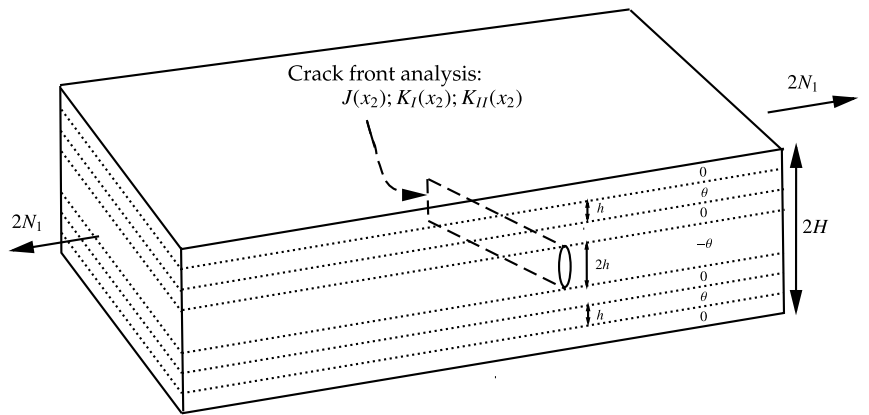
(a) Full-thickness model including the crack front.

(b) Half-thickness model without the crack front.

Fig. 1. Two 3D tunnel crack models with definitions of load, geometry and two coordinate systems (x_1, x_2, x_3), $(x_L, x_T, x_{T'})$.

where $\lambda = E_T / E_L$ and $\rho = \frac{\sqrt{2E_L E_T}}{2G_{LT}} - \sqrt{\nu_{LT}\nu_{TL}}$ [19]. Exploiting symmetry in Fig. 1b, the average energy release rates in Mode I and Mode II, respectively, are calculated as

$$\bar{G}_I = \frac{1}{2}\frac{1}{h}\int_{-h}^{0}\sigma_{TT}(x_2)\delta_n(x_2)dx_2 \;\; ; \qquad \bar{G}_{II} = \frac{1}{2}\frac{1}{h}\int_{-h}^{0}\tau_{LT}(x_2)\delta_t(x_2)dx_2 \tag{5}$$

where $\delta_n(x_2)$ and $\delta_t(x_2)$ denote the normal and tangential crack opening profiles, respectively, of the full-width crack (see Fig. 2b), while $\sigma_{TT}(x_2)$ and $\tau_{LT}(x_2)$ are the transverse normal and shear stresses, respectively, before initiation of the tunnel crack. It is noted, that since the crack considered is fully aligned with the longitudinal material direction denoted by subscript L the normal Mode I opening denoted by subscript n follows the material transverse direction denoted by subscript T and tangential Mode II opening denoted by subscript t follows the material longitudinal direction denoted by subscript L. The stress-state used to evaluate energy release rate is that existing in the absence of the specific tunnel crack analyzed. For a tunnel crack growing between neighboring cracks, this stress-field is found from a finite element solution, while for isolated tunnel cracks, the constant far-field stress in the off-axis ply is used. In this latter case, Eq. (5) can be written as

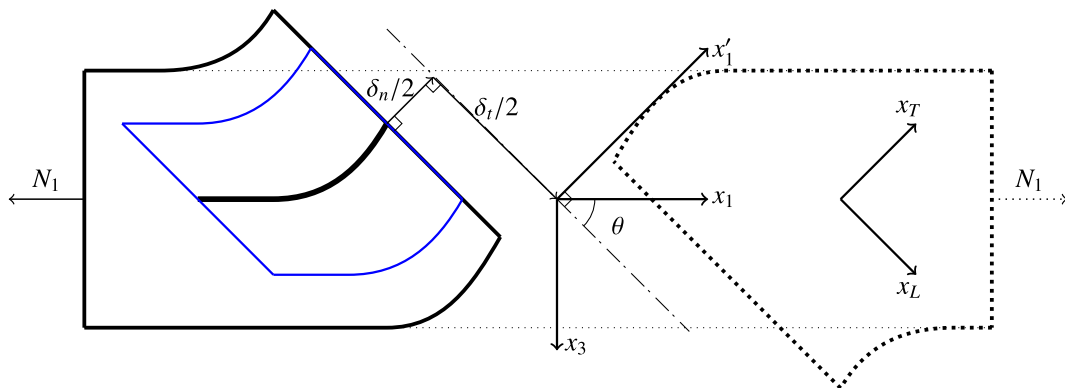$$\bar{G}_I = \frac{1}{2}\sigma_{TT}\bar{\delta}_n \; ; \;\; \bar{G}_{II} = \frac{1}{2}\tau_{LT}\bar{\delta}_t \tag{6}$$

where the average crack openings can be calculated from

$$\bar{\delta}_n = \frac{1}{h}\int_{-h}^{0}\delta_n(x_2)dx_2 \; ; \;\; \bar{\delta}_t = \frac{1}{h}\int_{-h}^{0}\delta_t(x_2)dx_2 \tag{7}$$
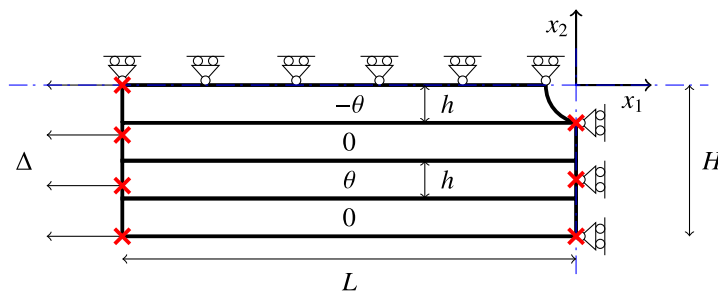
as done in Mikkelsen et al. [15].
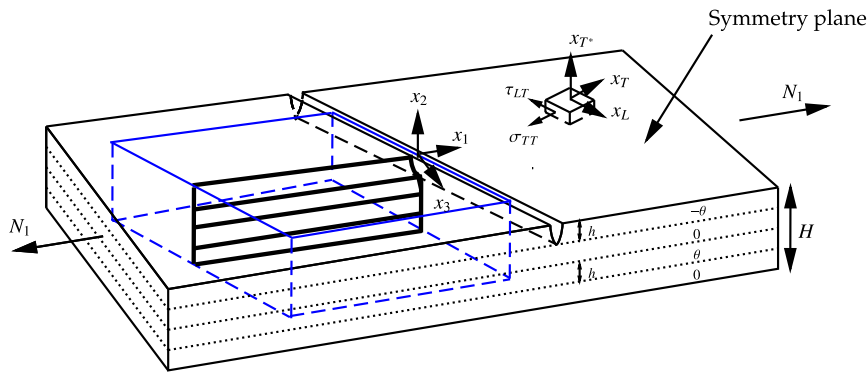
(a) Half-thickness model with an indication of the 2D model.

(b) Deformed symmetry plane, $x_2 = 0$, where bold black line indicates the upper edge of the 2D model.

(c) 2D model with elongation, Δ, symmetry ($x_2 = 0$) and anti-symmetry ($x_1 = 0$) boundary conditions.

Fig. 2. The 2D simplification of the tunnel crack problem.

3. Solution strategy

3.1. 2D formulation

Neglecting edge effects, the blue box in Fig. 2a indicates a domain in which the deformation state does not vary along the direction of the crack. Therefore, instead of finding the crack opening shape using the computationally expensive solution strategy in Quaresimin et al. [13], Mikkelsen et al. [15] and Bangaru et al. [16] to solve the full 3D model in Fig. 1b, the solution can be based on a much more efficient 2D formulation. Fig. 2b shows the top $x_1 - x_3$-plane at $x_2 = 0$ in an exaggerated deformed state where the blue lines indicate a top-view of the blue box from Fig. 2a.

The solution will be obtained on a 2D domain indicated by thick lines in Fig. 2a. In Fig. 2b this 2D domain is represented by a single thick line along the middle of the plate. The computational 2D domain is initially oriented along the main tensile direction x_1,

and hence, it is oriented at an angle θ relative to the tunnel crack. The size of the domain is given by the length in the x_1-direction, L and the half laminate height, H, as shown in Fig. 2c. Note that when referring to the x_i coordinate system, the displacement field within the 2D domain, u_i, will be three-dimensional except for specific values of θ, for which the solution will reduce to a planar displacement field.

The external far-field loading is prescribed as an elongation, Δ, in the x_1-direction along the edge $x_1 = -L$ as illustrated in Fig. 2c for $x_3 = 0$. The in-plane symmetries are imposed along $x_1 = 0$ for $x_2 \leq -h$ by $u_1 = 0$ and along $x_2 = 0$ by $u_2 = 0$ (see Fig. 2c). In addition, anti-symmetric boundary conditions in the out-of-plane direction need to be prescribed by zero displacements in the x_3-direction, $u_3 = 0$, along $x_1 = 0$ for $x_2 \leq -h$ and along $x_1 = -L$. This is illustrated by red crosses in Fig. 2c.

To accommodate such 3D deformations, a new coordinate axis perpendicular to the crack plane is defined as

$$x_1' = x_1 - x_3 \cot(\theta) \tag{8}$$

as also shown in Fig. 2b. For $\theta = 90°$ one has $x_1' = x_1$ where the formulation will simplify to a generalized plane strain formulation. For $\theta \in \,]0°; 90°[$, the unit of the x_1'-axis is stretched relative to that of the x_1-axis. For $\theta = 0°$, Eq. (8) is not defined. The total 3D displacement field, u_i, only depends on x_1' and x_2 and will here be expressed by the sum of that originating from a homogeneous far-field displacement gradient, $\bar{u}_{i,j}$, and a fluctuation field, $\tilde{u}_i$, that vanishes in the far-field

$$u_i[x_1, x_2, x_3] = \bar{u}_{i,j} x_j + \tilde{u}_i[x_1', x_2] \qquad ; \qquad i = 1, 2, 3 \tag{9}$$

The far-field small strain and rotations, resulting from the imposed far-field loading, are given as

$$\bar{\varepsilon}_{ij} = \frac{1}{2}(\bar{u}_{i,j} + \bar{u}_{j,i}) \qquad ; \qquad \bar{\omega}_{ij} = \frac{1}{2}(\bar{u}_{i,j} - \bar{u}_{j,i}) \tag{10}$$

Without loss of generality, and consistent with the boundary conditions discussed above, we take $\bar{\omega}_{ij} = 0$, implying that $\bar{u}_{i,j} = \bar{u}_{j,i}$. The gradients of the total displacement field, u_i, are then given by

$$\begin{aligned}
u_{i,\alpha} &= \bar{u}_{i,\alpha} + \tilde{u}_{i,\alpha} = \bar{\varepsilon}_{i\alpha} + \tilde{u}_{i,\alpha} \qquad ; \qquad \alpha = 1, 2 \\
u_{i,3} &= \bar{u}_{i,3} - \cot(\theta) \cdot \tilde{u}_{i,1} = \bar{\varepsilon}_{i3} - \cot(\theta) \cdot \tilde{u}_{i,1}
\end{aligned} \tag{11}$$

3.2. Element formulation

A special plane element with three translational displacements degrees of freedom, u_i, in each of the M nodes is developed. The element is derived in a general form to model the full six components of a 3D strain field. The finite element solution will be based on the displacement field on the plane $x_3 = 0$ in Fig. 2, at which

$$u_i[x_1, x_2, 0] = u_i[x_1, x_2] = \bar{u}_{i,\alpha} x_\alpha + \tilde{u}_i[x_1, x_2] \tag{12}$$

From Eq. (8) it follows that for $x_3 = 0$ one has $x_1' = x_1$ and $u_3 = \tilde{u}_3$. For the finite element implementation, the total in-plane displacements, $u_\alpha[x_1, x_2]$, and the fluctuation of the out-of-plane displacement, $\tilde{u}_3[x_1, x_2]$, are defined as the unknown fields. Following the decomposition of the displacement field, Eq. (9), and using Eq. (11) the small strain components are expressed by these unknown field variables as

$$\begin{aligned}
\varepsilon_{11} &= & \bar{\varepsilon}_{11} + \tilde{u}_{1,1} & & = u_{1,1} \\
\varepsilon_{22} &= & \bar{\varepsilon}_{22} + \tilde{u}_{2,2} & & = u_{2,2} \\
\gamma_{12} &= & 2\left\{\bar{\varepsilon}_{12} + \frac{1}{2}(\tilde{u}_{1,2} + \tilde{u}_{2,1})\right\} & & = u_{1,2} + u_{2,1} \\
\gamma_{13} &= & 2\left\{\bar{\varepsilon}_{13} + \frac{1}{2}(-\cot(\theta) \cdot \tilde{u}_{1,1} + \tilde{u}_{3,1})\right\} & & = \bar{\gamma}_{13} + \cot(\theta) \cdot \bar{\varepsilon}_{11} - \cot(\theta) \cdot u_{1,1} + \tilde{u}_{3,1} \\
\gamma_{23} &= & 2\left\{\bar{\varepsilon}_{23} + \frac{1}{2}(-\cot(\theta) \cdot \tilde{u}_{2,1} + \tilde{u}_{3,2})\right\} & & = \bar{\gamma}_{23} + \frac{1}{2}\cot(\theta) \cdot \bar{\gamma}_{12} - \cot(\theta) \cdot u_{2,1} + \tilde{u}_{3,2} \\
\varepsilon_{33} &= & \bar{\varepsilon}_{33} + \tilde{u}_{3,3} & & = \bar{\varepsilon}_{33} - \cot(\theta) \cdot \tilde{u}_{3,1}
\end{aligned} \tag{13}$$

Here, the engineering shear strains are introduced as twice the tensorial shear strains, i.e. $\gamma_{12} = 2\varepsilon_{12}, \gamma_{13} = 2\varepsilon_{13}$ and $\gamma_{23} = 2\varepsilon_{23}$. Using Voigt notation, the strain vector, ε, can be found based on the element displacement vector, D, for an element with M nodes, as

$$\begin{aligned}
\varepsilon &= BD \\
\varepsilon^T &= \{\varepsilon_{11}, \varepsilon_{22}, \gamma_{12}, \gamma_{13}, \gamma_{23}, \varepsilon_{33}\}^T \\
D^T &= \{u_1^{(1)}, u_2^{(1)}, \tilde{u}_3^{(1)}, \dots u_1^{(M)}, u_2^{(M)}, \tilde{u}_3^{(M)}, \bar{\varepsilon}_{11}, \bar{\gamma}_{12}, \bar{\gamma}_{13}, \bar{\gamma}_{23}, \bar{\varepsilon}_{33}\}^T
\end{aligned} \tag{14}$$

with the element strain–displacement matrix

$$B = \begin{bmatrix}
N_{1,1} & 0 & 0 & \dots & N_{M,1} & 0 & 0 & 0 & 0 & 0 & 0 & 0 \\
0 & N_{1,2} & 0 & \dots & 0 & N_{M,2} & 0 & 0 & 0 & 0 & 0 & 0 \\
N_{1,2} & N_{1,1} & 0 & \dots & N_{M,2} & N_{M,1} & 0 & 0 & 0 & 0 & 0 & 0 \\
-c' N_{1,1} & 0 & N_{1,1} & \dots & -c' N_{M,1} & 0 & N_{M,1} & c' & 0 & 1 & 0 & 0 \\
0 & -c' N_{1,1} & N_{1,2} & \dots & 0 & -c' N_{M,1} & N_{M,2} & 0 & \frac{1}{2}c' & 0 & 1 & 0 \\
0 & 0 & -c' N_{1,1} & \dots & 0 & 0 & -c' N_{M,1} & 0 & 0 & 0 & 0 & 1
\end{bmatrix} \tag{15}$$

Here, N_i for $i = 1 \dots M$ are the shape functions and $c' = \cot(\theta)$ for short. It is noted, that $\boldsymbol{B}$ is a $6 \times (3M + 5)$ matrix, where M is the number of nodes of the 2D element. Based on the principle of virtual work

$$\int_V \boldsymbol{\sigma} \delta \boldsymbol{\varepsilon} \mathrm{d}V = \int_S \boldsymbol{T} \delta \boldsymbol{u} \mathrm{d}S \tag{16}$$

the element stiffness matrix, $\boldsymbol{K}$, can then be established in the usual manner as

$$\boldsymbol{K} = \int_V \boldsymbol{B}^T \boldsymbol{E} \boldsymbol{B} \mathrm{d}V = t \int_A \boldsymbol{B}^T \boldsymbol{E} \boldsymbol{B} \mathrm{d}A \tag{17}$$

where t is the unit thickness of the element, while $\boldsymbol{E}$ is the 6×6 constitutive matrix determined by Young's moduli, shear moduli and Poisson's ratios,

$$\boldsymbol{E} = \boldsymbol{T_1}(\theta)^{-1} \begin{bmatrix} E_L(1 - v_{TT'}v_{T'T})\alpha & E_L(v_{TL} + v_{TT'}v_{T'L})\alpha & 0 & 0 & 0 & E_L(v_{T'L} + v_{TL}v_{T'T})\alpha \\ & E_T(1 - v_{LT'}v_{T'L})\alpha & 0 & 0 & 0 & E_T(v_{T'T} + v_{LT}v_{T'L})\alpha \\ & & G_{LT} & 0 & 0 & 0 \\ & & & G_{LT'} & 0 & 0 \\ & & & & G_{TT'} & 0 \\ \text{symmetric} & & & & & E_{T'}(1 - v_{LT}v_{TL})\alpha \end{bmatrix} \boldsymbol{T_2}(\theta) \tag{18}$$

Here,

$$\alpha = \frac{1}{1 - v_{LT}v_{TL} - v_{TT'}v_{T'T} - v_{T'L}v_{LT'} - 2v_{TL}v_{T'T}v_{LT'}}$$

and, $\boldsymbol{T_1}(\theta)$ and $\boldsymbol{T_2}(\theta)$ are the transformation matrices between the material coordinate system $(x_L, x_T, x_{T'})$ and x_i, which depend on θ in each individual layer. The transformation matrices are given as

$$\boldsymbol{T_1}(\theta)^{-1} = \begin{bmatrix} c^2 & 0 & 0 & 2sc & 0 & s^2 \\ 0 & 1 & 0 & 0 & 0 & 0 \\ 0 & 0 & c & 0 & s & 0 \\ -sc & 0 & 0 & c^2 - s^2 & 0 & sc \\ 0 & 0 & -s & 0 & c & 0 \\ s^2 & 0 & 0 & -2sc & 0 & c^2 \end{bmatrix} \quad ; \quad \boldsymbol{T_2}(\theta) = \begin{bmatrix} c^2 & 0 & 0 & -sc & 0 & s^2 \\ 0 & 1 & 0 & 0 & 0 & 0 \\ 0 & 0 & c & 0 & -s & 0 \\ 2sc & 0 & 0 & c^2 - s^2 & 0 & -2sc \\ 0 & 0 & s & 0 & c & 0 \\ s^2 & 0 & 0 & sc & 0 & c^2 \end{bmatrix} \tag{19}$$

where $c = \cos(\theta)$ and $s = \sin(\theta)$. The constitutive matrix defines the relation between stresses, $\boldsymbol{\sigma}$, and strains, $\boldsymbol{\varepsilon}$, through

$$\boldsymbol{\sigma} = \boldsymbol{E} \boldsymbol{\varepsilon}. \tag{20}$$

It is noted, that for $\theta = 90°$ a generalized plane strain element is recovered where the out-of-plane strain ε_{33} will have a constant value equal to $\bar{\varepsilon}_{33}$. Beuth [5] and Ho and Suo [6] based their analysis on a plane strain model with $\varepsilon_{33} \equiv 0$.

4. User element implementation

The developed element is implemented in ABAQUS through a user element (UEL) subroutine. The results can be visualized conveniently using shadow elements based on a user material (UMAT) subroutine (see [20]). The preprocessing is based on a Python script, which creates the geometry, model properties, the load, and displacement boundary conditions. Then an input file for ABAQUS is generated and automatically modified to include the user element subroutine. The input file is submitted and finally, the Python script continues with the post-processing to compute the crack profile and the energy release rate. The Fortran code for the UEL and the UMAT based "shadow element" as well as the Python scripts used for the simulations, can be obtained from Mikkelsen et al. [17].

4.1. User element subroutine

The UEL subroutine is called by each element and requires the definition of the stiffness matrix $\boldsymbol{K}$ and the residual vector. The stiffness matrix $\boldsymbol{K}$ can be found by evaluating the integral (17) using Gauß integration. The residual vector is then found by multiplying the stiffness matrix with the displacement and far-field strain vector $\boldsymbol{D}$. Finally, the stresses and strains at the Gauß points are calculated with Eqs. (14) and (20).

4.2. Strain prescription to all nodes

The presented element formulation poses implementational challenges in commercial codes, due to the additional and unconventional degrees of freedom regarding the far field strains, $\bar{\varepsilon}$. In the formulation of the special element strain–displacement-matrix, $\boldsymbol{B}$ in Eq. (15), the strains, $\bar{\varepsilon}$, of the homogeneous far-field are to be applied as additional degrees of freedom common to all the elements.

In the case studied here of the symmetric and balanced laminate under in-plane loading in the (x_1, x_3)-plane the implementation can be simplified. Here, the only non-zero strains of the homogeneous far field are $\bar{\varepsilon}_{11}$ and $\bar{\varepsilon}_{33}$. As the tunneling cracks inside the laminates have a negligible influence on the far-field, the homogeneous far-field strains can be approximated by classical laminate

theory and the corresponding additional far-field degrees of freedom can be eliminated. This step is done to simplify the element implementation. Note, that adding the additional degrees of freedom concerning the far-field in the element formulation instead of estimating the far field beforehand will yield identical results.

Thus the far-field average strains are calculated during pre-processing with classical laminate theory, and are thus known. The strain–displacement matrix can then be included in the UEL subroutine in the following form

$$\boldsymbol{B} = \begin{bmatrix} N_{1,1} & 0 & 0 & \dots & N_{M,1} & 0 & 0 & 0 & 0 \\ 0 & N_{1,2} & 0 & \dots & 0 & N_{M,2} & 0 & 0 & 0 \\ N_{1,2} & N_{1,1} & 0 & \dots & N_{M,2} & N_{M,1} & 0 & 0 & 0 \\ -c'N_{1,1} & 0 & N_{1,1} & \dots & -c'N_{M,1} & 0 & N_{M,1} & c' & 0 \\ 0 & -c'N_{1,1} & N_{1,2} & \dots & 0 & -c'N_{M,1} & N_{M,2} & 0 & 0 \\ 0 & 0 & -c'N_{1,1} & \dots & 0 & 0 & -c'N_{M,1} & 0 & 1 \end{bmatrix}. \tag{21}$$

Furthermore, an element displacement vector is defined with size $(3M + 2) \times 1$, where the last two rows represent the far-field homogeneous strain field. This is then used to calculate the stiffness matrix, $\boldsymbol{K}$ in Eq. (17), the residual vector, as well as the strains and the stresses. The contributions from the known far-field strains are moved to the residual vector via multiplication of the stiffness matrix with the element displacement vector and subsequent subtraction of the entries related to the far-field strains. Subsequently, the matrices and vectors are shortened to exclude entries corresponding to the homogeneous strain field. The shortened matrix and vector are then used by ABAQUS to compute the displacements.

4.3. Shadow elements

The visualization of the results of a UEL subroutine requires an additional step. By default, ABAQUS is only able to illustrate the nodal displacements of a UEL but is not able to interpret the field values inside the element, as neither the interpolation nor the location of the Gauß points is known by the post-processing tool in ABAQUS.

A solution to this is using similar standard elements from the ABAQUS library — here referred to as shadow elements (see [20]). The standard elements must have the same Gauß point locations and numbering as the element developed. A secondary identical mesh has to be created using the standard elements. The standard elements use the same nodes as the UEL, so that the nodal results in terms of displacements and reaction forces, can be transferred. This allows for a visualization of the displacement field.

The stresses and strains are transferred with a UMAT subroutine through a Fortran common-block from the UEL subroutine. In the UMAT subroutine, a zero stiffness constitutive model leads to a zero stiffness matrix. This ensures, that the material subroutine does not modify any values of the UEL subroutine. In the material subroutine, the stresses and strains are stored as state variables instead of the built-in stress and strain variables, as this would require the same number of stress and strain variables for both the user-defined and built-in standard elements. Hereby the stress and strain field can be visualized.

There are two limitations of this shadow element technique. First, it requires that there exists a similar element in the ABAQUS standard library in terms of the number of nodes — for the purpose of the present analyses, the element used was an 8-noded membrane element (M3D8) which has 3 nodal degrees of freedom. The other limitation is that the computational time is increased significantly due to the inclusion of the UMAT. Therefore, it can be beneficial in the code to turn the shadow elements on and off depending on the specific needs for visualization of the displacement field and state variables.

4.4. Input file

The input file defines the model that is to be solved. It is generated by ABAQUS after preprocessing and can then be submitted for solving. The inclusion of the UEL requires a modification of the input file, as the UEL has to be defined and assigned to the individual elements, together with the specific UEL inputs in terms of far-field strains. Subsequently, copies of all UEL have to be created in relation to the specified shadow elements. These operations are built into a Python script.

4.5. Python script

The Python script automates the entire process and can be run through ABAQUS to calculate the energy release rate and crack profiles. It includes the pre-processing to create the model and calculation of the homogeneous far-field strains from laminate theory. Furthermore, the generation and modification of the input file, solving, and post-processing for obtaining the energy release rate are included. The script requires the geometrical dimensions, material properties, and loading. This enables an efficient method for carrying out systematic parametric studies.

5. Material systems

Three glass fiber composites (GlassFRP1, GlassFRP2, and GlassFRP3) and two carbon fiber composites (CarbonFRP1 and CarbonFRP2) will be considered in the analyses of a laminate layup $[0/\theta/0/ - \theta]_s$, (see Table 1). The material stiffness values are taken from Quaresimin et al. [13], Mikkelsen et al. [15] and Bangaru et al. [16] in order to be able to validate the 2D model predictions with the 3D simulations from those earlier studies.

Table 1
Material systems used.

Material unit	E_L [GPa]	$E_T = E_{T'}$ [GPa]	$v_{LT} = v_{LT'}$ [−]	$v_{TT'}$ [−]	$G_{LT} = G_{LT'}$ [GPa]	$G_{TT'}$ [GPa]	λ [−]	ρ [−]
GlassFRP1	30.6	8.62	0.29	0.33	3.25	2.90	0.282	2.34
GlassFRP2	41.2	10.3	0.26	0.41	3.79	3.66	0.250	2.59
GlassFRP3	40.3	12.3	0.27	0.40	4.62	4.38	0.305	2.26
CarbonFRP1	126	7.56	0.26	0.40	3.69	2.70	0.060	4.12
CarbonFRP2	266	5.49	0.27	0.40	3.54	2.37	0.021	5.36
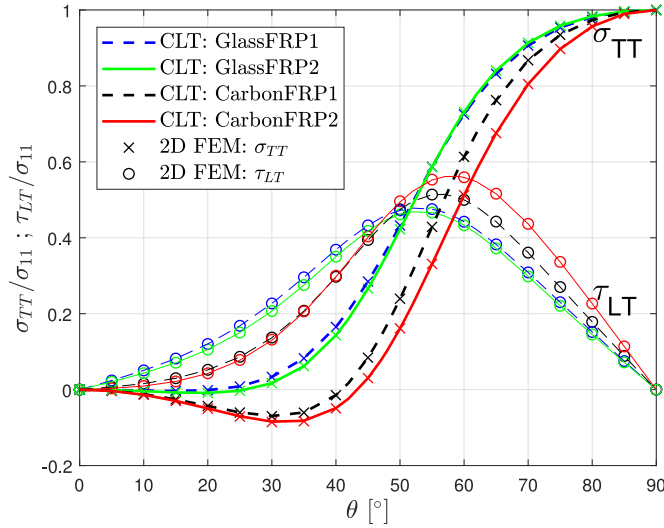
Fig. 3. The transverse and shear stresses (marks) in the central non-cracked off-axis layer compared with the values (lines) extracted from a Classical Laminate Theory (CLT).

The out-of-plane element coordinate direction, x_3, in the 2D off-axis finite element formulation is aligned with the orientation of the center off-axis ply. Thereby, the stress components in the finite element solution will be given directly in these off-axis material orientations. Fig. 3 shows the stress components in the normal direction to the fiber orientation, σ_{TT}, and the shear stress, τ_{LT}, for cases without any cracks. For the cases with cracks to be studied, these two stress components are required in Eqs. (5) and (6) for calculating the average steady-state energy release rate and mode-mixity for a tunnel crack in this layer using the energy balancing method. For validating the ABAQUS UEL implementation of the off-axis 2D finite element formulation, the predicted stress components have been compared with a Classical Laminate Theory (CLT) in Fig. 3, and a very good agreement for all the cases analyzed is found.

6. Results

The material systems studied here (see Table 1) were also considered by Quaresimin et al. [13], Mikkelsen et al. [15] and Bangaru et al. [16] in 3D. Hence, direct validation of the novel 2D formulation against the full 3D model is possible. In the following, this will be done for a number of cases.

6.1. Uniaxially loaded off-axis tunnel-crack

Fig. 4 shows the out-of-plane displacement, and the out-of-plane normal strain component found from the 2D finite element solution near the tunnel crack, for the material system GlassFRP1 with the layup angle $\theta = 45°$. Fig. 4a shows the full 2D model with contours of the normalized out-of-plane displacement, $u_3/\bar{\varepsilon}_{11}$, Fig. 4b shows a close-up view with the mesh of Fig. 4a near the crack, and Fig. 4c shows the same close-up view, but with contours of normalized out-of-plane strain, $\varepsilon_{33}/\bar{\varepsilon}_{11}$. As the simulations are based on a linear finite element model, a scaling factor is chosen for the in-plane deformation field in order to have a visible crack opening in Fig. 4. Despite being a 2D finite element model, the off-axis finite element formulation is able to correctly predict the out-of-plane displacements, u_3, which are included as additional degrees-of-freedom in the finite element formulation, as well as the out-of-plane strain $\varepsilon_{33} = \bar{\varepsilon}_{33} - \cot(\theta) \cdot \tilde{u}_{3,1}$ (see Eq. (13)), where $\bar{\varepsilon}_{33}$ (and $\bar{\varepsilon}_{11}$) is found from Classical Laminate Theory. In this specific case, $\bar{\varepsilon}_{33}/\bar{\varepsilon}_{11} = -0.452$. Both the displacement field and the strain field exhibit a localized deformation around the tunnel crack while they represent homogeneous deformation in the major part of the model. The solution obtained has been found to agree
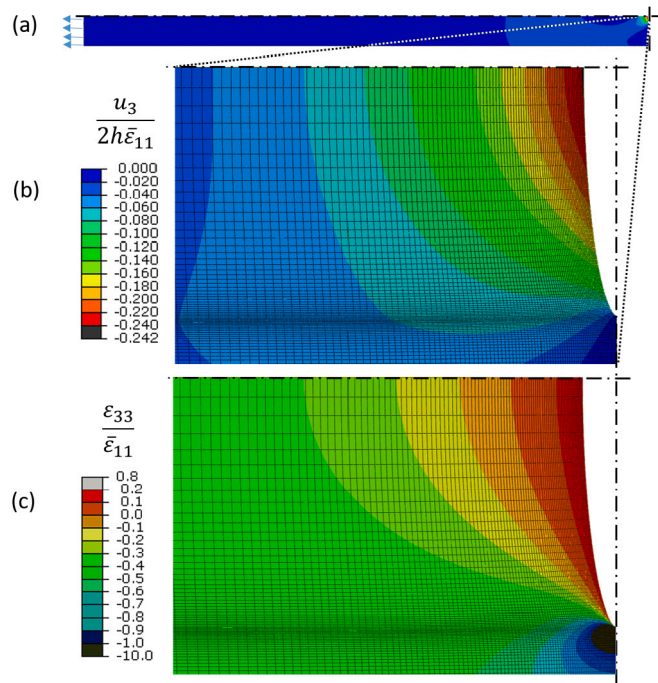
Fig. 4. Deformed mesh and contour plots for a uniaxially loaded off-axis crack predicted for the material system GlassFRP1 with the layup angle $\theta = 45°$. (a) The full 2D model with the contours of the normalized out-of-plane displacement, $u_3/(2h\bar{\varepsilon}_{11})$, (b) a close-up view of the solution from (a) near the crack, and (c) the same close-up view now showing the normalized out-of-plane strain $\varepsilon_{33}/\bar{\varepsilon}_{11}$. The maximum displacement value at the crack is $(u_1^{max}; u_3^{max})/(2h\bar{\varepsilon}_{11}) = (-0.691; -0.242)$. The normalized far-field out-of-plane strain found using the Classical Laminate Theory is $\bar{\varepsilon}_{33}/\bar{\varepsilon}_{11} = -0.452$.
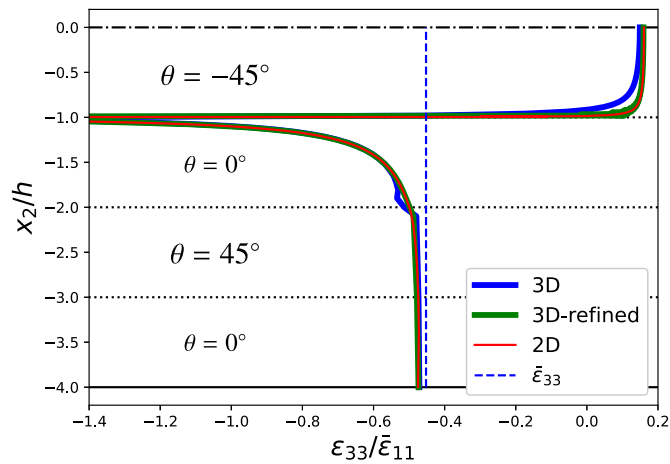

Fig. 5. 2D versus 3D comparison of the variation of ε_{33} along the x_2-axis. Two 3D meshes with a different degree of refinement are presented. For both meshes, the displacements and the energy release rates have converged, however minor differences in the strain field are observed. The refined 3D mesh shows good agreement with the 2D solution using a similar element length L_{el} in the x_1-direction.

well with the full 3D finite element prediction with a maximum out-of-plane deflection of $(u_1^{max}; u_3^{max})/(2h\bar{\varepsilon}_{11}) = (-0.691; -0.242)$ at the point with maximum normal crack opening.

In Fig. 5, the 2D off-axis finite element-based solution of the normalized out-of-plane normal strain ε_{33} is compared to the corresponding full 3D finite element predictions in detail. The solution in Fig. 5 is shown along a path following the x_2-axis in the undeformed finite element mesh. The horizontal black lines in Fig. 5 indicate the ply interfaces (dotted) as well as the symmetry line for the central ply (dash-dotted) and the lower outer surface (solid). Together with the two strain solutions, the average out-of-plane strain, $\bar{\varepsilon}_{33}$, obtained from the classical laminate theory, is also shown. The difference between $\bar{\varepsilon}_{33}$ and the 2D ε_{33} is given by the term $\cot(\theta) \cdot \tilde{u}_{3,1}$ (see Eq. (13)). A good overall agreement is found between the 2D and 3D models. Nevertheless, there can be seen some difference between the strain field from the 2D and 3D solution along the crack front (the top-ply). This is due to the strain
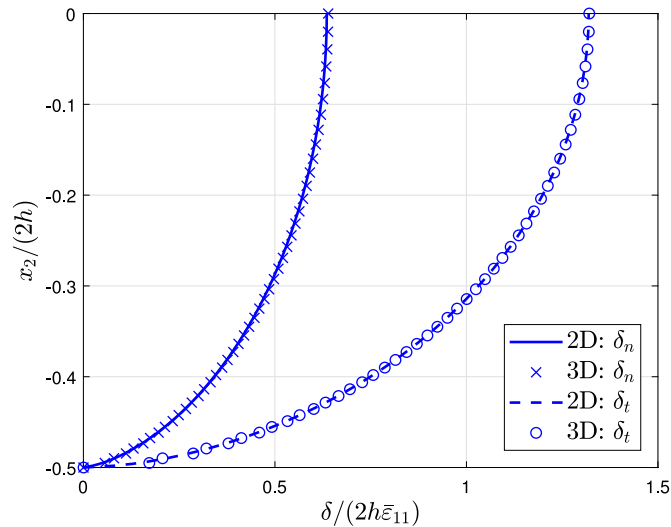
Fig. 6. Comparing the normal, δ_n, and tangential, δ_t, crack opening displacement profile for the GlassFRP1 case with $\theta = 45°$, see Fig. 2b. The lines are from the 2D off-axis finite element, the circular and cross marks are from the 3D simulation performed in Mikkelsen et al. [15].

Table 2
Numerical comparison of uniaxial loaded off-axis tunnel-crack for GlassFRP1 with $\theta = 45°$.

Material case	θ	CLT		FEM						
		$\dfrac{\sigma_{TT}}{\sigma_{11}}$	$\dfrac{\tau_{LT}}{\sigma_{11}}$		$\dfrac{\delta_n}{2h\bar{\varepsilon}_{11}}$	$\dfrac{\delta_t}{2h\bar{\varepsilon}_{11}}$	$\dfrac{\bar{G}_I}{2h\bar{\varepsilon}_{11}\sigma_{11}}$	$\dfrac{\bar{G}_{II}}{2h\bar{\varepsilon}_{11}\sigma_{11}}$	$\dfrac{\bar{G}_{ss}}{2h\bar{\varepsilon}_{11}\sigma_{11}}$	$\bar{\psi}$
GlassFRP1	45°	0.2847	0.4327	2D:	0.4792	1.0150	0.0682	0.2196	0.288	67.9°
				3D:	0.4822	1.0164	0.0686	0.2199	0.289	67.9°

values from the finite element solution being extrapolated from the finite element integration points to the crack surface where the element size in the 2D mesh, $L_{el} \times h_{el} = 0.004h \times 0.004h$, is 1/10th of the element length used in the 3D mesh and therefore leads to a much more accurate extrapolation in the 2D model. The jump in the strain prediction between the second and third ply in the 3D solution is due to a use of a much coarser mesh in the two lower plies attached to the two upper plies with a tie constraint between the two incompatible meshes. To verify that this is the reason, a second analysis with a refined 3D mesh using a similar resolution as the 2D model is conducted, showing a good agreement with the 2D solution. However, the quantities of interest, the crack opening displacement, seen in Fig. 6 and energy release rate have already converged for the coarser 3D mesh. Thus the coarse 3D mesh is deemed sufficient and used for the remaining studies.

Regarding the computational effort, the refined 3D model uses almost 25′000′000 degrees of freedom, and the coarse 3D model uses about 11′000′000 degrees of freedom with computational times ranging between 2 and 5 h using 200 CPUs, as shown in [15]. In contrast, the fine 2D model with 31′000 degrees of freedom only takes 5 s on a single CPU, leading to an estimated speed-up between three and four orders of magnitude.

Fig. 6 shows the detailed crack opening profile given by the normal opening, δ_n, and transverse opening, δ_t, using the definition given in Fig. 2b, which is found by a projection onto the crack normal in the $(x_1; x_3)$-plane. In the contour plot of Fig. 4 the maximum normalized crack opening displacement was found to be $(u_1^{max}; u_3^{max})/(2h\bar{\varepsilon}_{11}) = (-0.691; -0.242)$. This corresponds to a maximum crack opening of $(\delta_n^{max}; \delta_t^{max})/(2h\bar{\varepsilon}_{11}) = (0.635; 1.320)$, which coincides with the end-points of the curves in Fig. 6. In Fig. 6, the crack opening profile obtained from the 2D analysis is also compared to the profile found from the full 3D solution given in Mikkelsen et al. [15]. The lines in Fig. 6 show the predictions from the 2D off-axis finite element formulation while the circular markings and cross markings show the 3D prediction. The two solutions are found to coincide well along the entire crack opening profile.

In Table 2, the numerical values of the average crack openings calculated using Eq. (7) based on a full 3D simulation and the new 2D off-axis finite element simulation are compared. The difference is found to be less than 1.5%. Using Eq. (6), the average energy release rate in Mode I and Mode II can be calculated from the average crack opening and the stress-field in the un-cracked laminate. These values are also shown in Table 2 together with the average steady-state energy release rate, $\bar{G}_{ss}$, and average mode-mixity angle, $\bar{\psi}$, calculated using Eq. (3). Very good agreement has been found between all the values with less than 0.5% difference between the 2D and 3D results for the average steady-state energy release rate $\bar{G}_{ss}$ and the average mode-mixity $\bar{\psi}$.

Fig. 7 shows the average steady-state energy release rate, $\bar{G}_{ss}$, and the average mode-mixity, $\bar{\psi}$, for all the cases investigated in Mikkelsen et al. [15] using 3D finite element calculations. An excellent agreement is obtained, whilst saving more than four orders of magnitude in computational time using the novel 2D off-axis element.
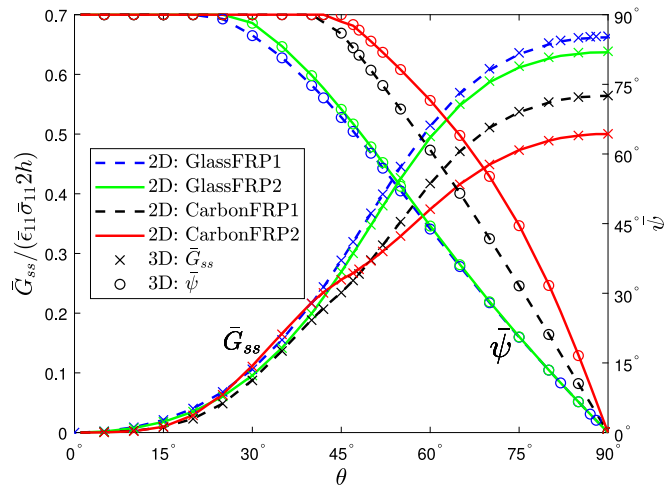
Fig. 7. The total average energy release rate, $\bar{G}_{ss}$, and average mode-mixity, $\bar{\psi}$, for the four material cases. The lines are from the 2D off-axis finite element, and the circular and cross marks are from the 3D simulations in Mikkelsen et al. [15].
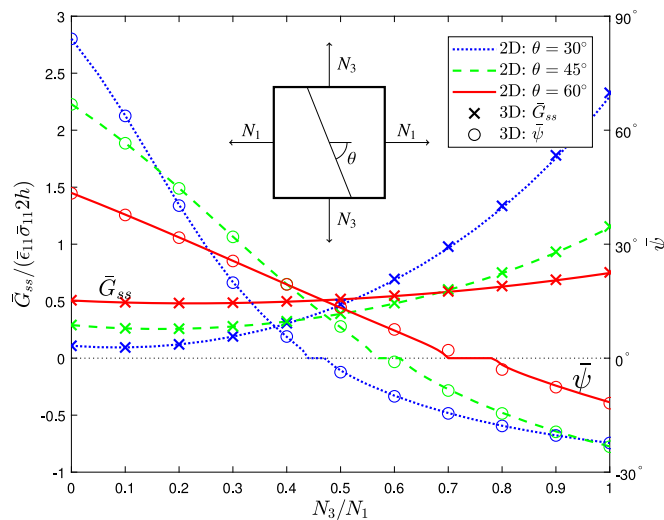

Fig. 8. The dependence of the average steady-state energy release rate $\bar{G}_{ss}$ and the average mode-mixity $\bar{\psi}$ on the load ratio N_3/N_1 for the GlassFRP3 case with $\theta \in [30, 45, 60]°$. The points indicate the 3D solution from Bangaru et al. [16] and the lines by the 2D prediction.

6.2. Biaxial loaded off-axis tunnel crack

An off-axis tunnel crack loaded biaxially was analyzed by Bangaru et al. [16]. The layup analyzed here is the same and the material system studied here is GlassFRP3 with the properties shown in Table 1. The biaxial loading is given by the two loads N_1 and N_3, and the effect of the biaxial loading ratio N_3/N_1 is investigated. Bangaru et al. [16] performing such an analysis based on a full 3D model applying a superposition of the average stress intensity factors K_I and K_{II}. Using the 2D off-axis finite element formulation, those corresponding simulations are sufficiently fast that all the load cases considered here are simulated directly applying the different load ratios N_3/N_1. The out-of-plane loading is applied in the 2D off-axis finite element model through the $\bar{\varepsilon}_{33}$ value which together with $\bar{\varepsilon}_{11}$ is determined from the classical laminate theory. Note that the applied axial deformation Δ along the outer boundary should correspond to $\bar{\varepsilon}_{11}$ calculated from Classical Laminate Theory.

Fig. 8 shows the average steady-state energy release rate, $\bar{G}_{ss}$, and the average mode-mixity, $\bar{\psi}$, predicted for biaxial load ratios in the range $N_3/N_1 \in [0; 1]$ for three different layups with $\theta = 30°$, $\theta = 45°$ and $\theta = 60°$. The load ratio $N_3/N_1 = 0$ corresponds to the uniaxial loaded off-axis tunnel crack analyzed in the previous sub-section. Similarly to Fig. 7, the curves in Fig. 8 are the predictions using the 2D off-axis finite element, while the circular and cross marks are predictions taken from the full 3D finite element simulations performed in Bangaru et al. [16]. As for the uni-axial load case shown in Fig. 7, a good agreement is also obtained using the 2D off-axis finite element method.

Comparing the predictions from the three different layup angles in Fig. 8, the blue curves for the smallest layup angle, $\theta = 30°$, show the largest sensitivity to a change in the biaxial loading ratio on both the energy release rate and the mode-mixity. For the uniaxial loading case, corresponding to $N_3/N_1 \equiv 0$, this layup angle has the lowest predicted energy release rate together with a high mode-mixity angle corresponding to a Mode II ($\bar{\psi} \simeq 85°$) dominated loading. This implies that a tunnel-crack is resilient to growth as the required energy release rate normally increases significantly when approaching Mode II crack tip loading, see e.g. Sørensen and Jacobsen [21]. Nevertheless, applying an additional transverse load, N_3, to the laminate, both a significant increased energy release rate, $\bar{G}_{ss}$, and a significant decreased mode-mixity, $\bar{\psi}$, approaching pure Mode I ($\bar{\psi} \simeq 0$) loading for $N_3/N_1 \approx 0.45$, is achieved. For a further increased transverse load, the mode-mixity becomes negative according to Fig. 8, implying that K_{II} in Eq. (2) is negative as K_I will always be positive. This effect follows from the change in direction of the shear stresses in the cracked laminate introduced by the N_3 loading as discussed by Bangaru et al. [16]. The change of sign indicates a shift in the direction of the shear loading between the crack surfaces going from a shear stress dominated by the N_1-loading to a shear stress dominated by the N_3-loading. In the numerical analysis, both the shear stress τ_{LT} and the shear crack opening δ_t will change sign while the Mode II contribution to the energy release rate G_{II} will remain positive. As the mode-mixity in the present work is calculated from the inherently positive energy release rates using Eq. (3), this change of sign must be defined differently, and hence the mode-mixity shown in Fig. 8 is defined as

$$\bar{\psi} = \frac{\tau_{LT}}{|\tau_{LT}|} \arctan\left(\lambda^{-1/4} \sqrt{\frac{\bar{G}_{II}}{\bar{G}_I}} \right) \tag{22}$$

where the sign of $\bar{\psi}$ is defined by the sign of τ_{LT} similarly to [16].

For a small θ-interval, τ_{LT} and $\bar{\delta}_t$ have been observed to have opposite signs resulting in a negative $\bar{G}_{II}$ contribution when using Eq. (6). Obviously, a negative energy release rate is non-physical and will also result in an undefined mode-mixity value-based in Eq. (22). Nevertheless, the negative Mode II energy contributions, $\bar{G}_{II}$, are for all cases numerically very small compared with the corresponding Mode I component, $\bar{G}_I$. Hence, in these cases, the mode-mixity angles θ have been defined to be pure Mode I resulting in small horizontal curve segments in Fig. 8 where $\bar{\psi} \equiv 0°$. A similar observation was made based on simulations by the 3D model used in Bangaru et al. [16], although the method employed there based on average stress intensity factors does not lead to negative values of $\bar{G}_{II}$. Despite the non-physical negative value of $\bar{G}_{II}$ in a very small region it is considered to have only a minor influence on the predictions. As discussed in Mikkelsen et al. [15] the splitting of the steady-state energy release rate into a Mode I and Mode II part cannot be established rigorously, but was found to give a good approximation of the mode-mixity obtained using an accurate crack-tip analysis. Therefore, the horizontal lines segments for the mode-mixity $\bar{\psi}$ in Fig. 8, should be considered as the consequence of the non-rigorous Mode I and Mode II split and will therefore not be a behavior with physical relevance.

6.3. Thickness dependency of the off-axis tunnel-crack

The effect of the ply thickness has been investigated by Crossman and Wang [22] for tunneling cracking at 90° using generalized plane strain models. Also, in Mikkelsen et al. [15], a limited study of the influence of the ply thickness on the energy release rate was performed under uniaxial loading with arbitrarily oriented cracks. However, due to the increasing numerical demands in the full 3D model, especially for an increasing H/h aspect ratio, only a few cases were analyzed. Now, using the novel 2D off-axis finite element formulation, an extensive parameter study can be performed.

Fig. 9 shows the thickness dependence of the energy release rate and the mode-mixity for the two material systems GlassFRP1 and CarbonFRP2 for layups with the angles $\theta = [30°, 45°, 60°, 90°]$. Five 3D solutions for the GlassFRP1 material system with $\theta = 45°$ simulated using the full 3D model for GlassFRP1 by Mikkelsen et al. [15] are also included for comparison in Fig. 9 as blue cross-marks. A good agreement between the full 3D and the new 2D finite element predictions can be observed. Despite the fact that the thickness dependence is found to be rather limited for the glass fiber cases, the carbon fiber case shows a significant variation for the layup angles $\theta = 30°$ and $\theta = 45°$ with a reduction of the steady-state energy release rate of about 80%–90% when comparing very thin ($h \ll H$) off-axis plies with equally thick plies. Both those two layup angles are cases where the crack-tip loading is pure Mode II with compressive normal loading over the crack surfaces. The decreasing energy release rates for thin off-axis plies with small off-axis angles are of high technical relevance when designing backing layers in non-crimp fabrics-based composites as tunnel-cracks in the off-axis backing bundles have been observed to be fatigue damage initiation sites in high cycle tension–tension cyclic loading (see [23,24]). Fig. 9b shows the corresponding change in the mode-mixity for the cases analyzed. All the cases show a reduction of the mode-mixity angle when reducing the off-axis ply thickness. A reduction, which is most significant for the GlassFRP1 case with a predicted mode-mixity decrease of up to 15° for thin plies in a $\theta = 30°$ off-axis layup. As a decreasing mode-mixity typically will decrease the critical energy release rate for the material (see e.g. Sørensen and Jacobsen [21]), the required energy release rate for crack growth will decrease. Hence, whether the decreasing energy release rate, which has been predicted for decreasing ply thicknesses, actually will result in a lower tendency of the laminate to form tunnel cracks will depend on how sensitive those cracks are on the corresponding decrease in the mode-mixity.

6.4. Effect of neighboring cracks

For all the analyses performed so far, the tunnel-crack is assumed to be isolated from neighboring cracks. Typically, this will only be the case during the initial phase of tunnel cracking. Later, when multiple tunnel-cracks are present, they will shield the stress-field in a neighboring region, thus lowering the energy available for nearby tunnel-cracking. Hutchinson and Suo [7] investigated
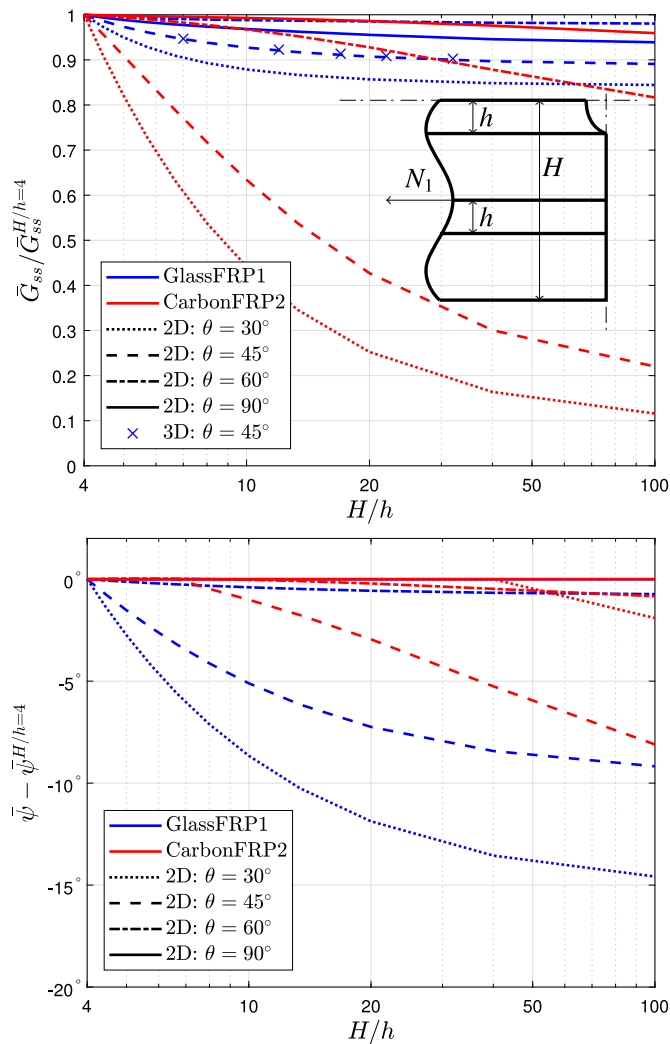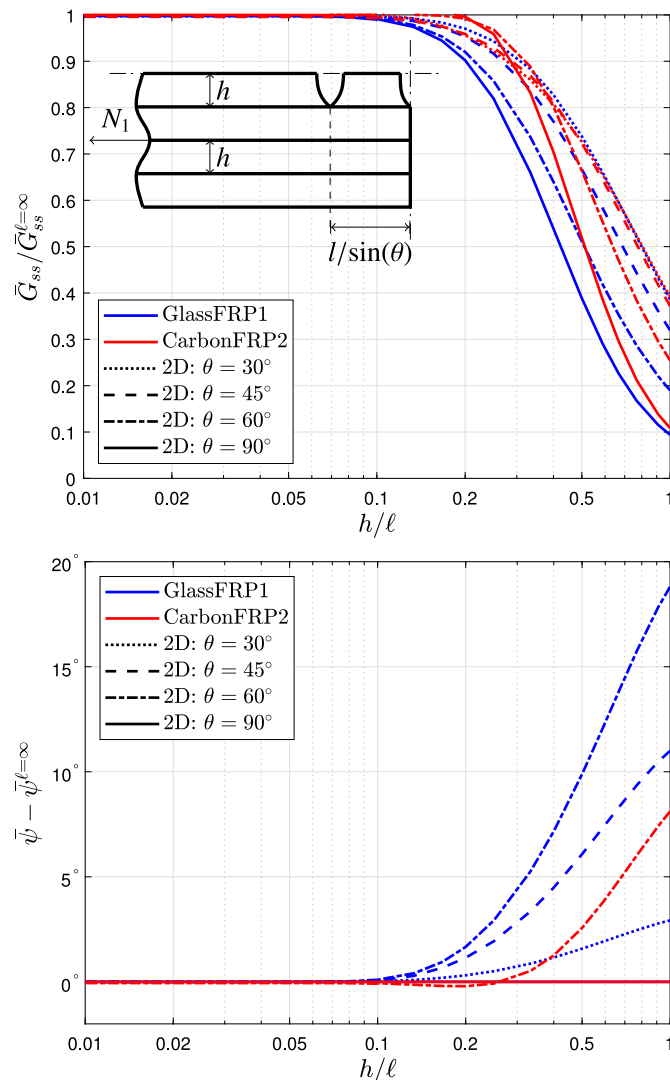
Fig. 9. The dependence of the steady-state energy release rate on the ratio between the laminate thickness and the ply thicknesses for the four layup angles $\theta = [30, 45, 60, 90]°$ for the two material systems GlassFRP1 and CarbonFRP2.

this saturation effect for 90° tunnel cracks using a 2D plane strain model while Quaresimin et al. [13] and Mikkelsen et al. [15] investigated a few cases using a full 3D finite element model for the off-axis case.

For uniaxial loading, Fig. 10 shows the influence of a neighboring crack on the energy release rate for the same two material cases and four layup angles as investigated in the previous subsection, i.e., $\theta \in [30°, 45°, 60°, 90°]$. The crack-spacing, ℓ, is defined as the normal distance between the cracks (see [13,15]). Due to symmetry, the cases studied here pertain to two pre-existing cracks and a tunnel crack growing in between at a distance, ℓ, to the existing cracks resulting in the crack spacing in the 2D off-axis finite element model given as $\ell / \sin \theta$ (see insert in Fig. 10). The presence of the neighboring cracks will result in an inhomogeneous stress-field in between the pre-existing cracks so that the stress-state cannot (as for the case of a single crack) be found from the Classical Laminate Theory. Hence, Eq. (6) cannot be used, but rather Eq. (5) with a through-thickness integration must be used. In order to perform the integration in Eq. (5), both the stress variation through the thickness before a crack has developed and the crack opening profile after the crack is fully developed is needed. This is obtained by solving the finite element model twice with two different boundary conditions along the crack-front at $x_1 = 0$. One model with $u_1 \equiv 0$ represents a configuration with no central crack for determining the stress-field, and one model with u_1 unconstrained represents a fully developed central crack for determining the crack opening. Therefore, each point on the curves shown in Fig. 10 is based on the results from two numerical solutions. Nevertheless, as each of these 2D solutions can be obtained in under a minute using a single CPU, all the curves can be established within a few hours of simulation time.

Fig. 10 shows the dependency of the crack spacing, ℓ, on the available energy release rate and mode-mixity. The energy release rate in Fig. 10a is normalized by the value obtained for an isolated crack, $\bar{G}_{ss}^{\ell=\infty}$, while the crack spacing is given by the ratio h/ℓ. A rather similar behavior is seen for all the analyzed cases where an influence from the neighboring crack is observed for a crack

Fig. 10. The dependence of the steady-state energy release rate and mode-mixity on the crack spacing for the GlassFRP1 and GlassFRP2 case with $\theta \in [30°, 45°, 60°, 90°]$.

spacing $\ell < 10h$ with a lowering of the available energy release rate of about 10% for a crack spacing of $h/\ell \in [0.2; 0.35]$. Similarly, the mode-mixity in Fig. 10b is seen to be significantly influenced for crack spacings less than about 10 ply thicknesses ($\ell < 10h$). With closely spaced neighboring cracks, the mode-mixity is seen to increase for all the cases analyzed, with the largest increase of almost 20° observed for the material case GlassFRP1 for the layup $\theta = 60°$. The results quantify a decreasing tendency for tunnel cracks to appear in between pre-existing tunnel cracks based on both the increasing mode-mixity and the decreasing energy release rate with h/ℓ.

7. Conclusion

In this study, it has been demonstrated for a symmetric and balanced laminate, that it is possible to obtain accurate predictions of the 3D deformation and strain-fields around an arbitrarily oriented tunnel-crack in an arbitrary ply layup using a specialized off-axis 2D finite element model. The main advantage of the 2D formulation is the significantly reduced computational time of more than four orders of magnitude, enabling thorough parameter studies. The most prominent situations in which the model is not applicable are in the presence of edge-effects, cracks oriented in multiple directions, or in-depth investigations of the crack front. The reason is that in these cases, the assumption of a steady-state is violated. Thus, prior to applying the proposed method to other problems, the presence of a steady-state has to be ensured first.

The novel 2D model was implemented in the commercial finite element code ABAQUS using the user element interface. The accuracy was demonstrated for a number of different tunnel-crack cases. The code can be obtained from Mikkelsen et al. [17]

where a GitLab link to the newest version of the code can also be found. In addition to being able to reproduce results from 3D simulations, the computationally much more efficient method has enabled detailed studies of the dependence of the tunnel-cracking on both the ply thickness and crack distance.

In the present study, the new 2D model has been limited to analyzing the available energy release rate and mode-mixity for the growth of an arbitrarily oriented off-axis tunnel crack, using a linear elastic material model. However, the framework has a broad range of applicability. For instance, the modeling technique can be extended to include the effects of the randomness in the actual micro-structure on the stress and strain-fields by a detailed representation of the fiber reinforcement and voids as in Vajari et al. [25]. The formulation could also be extended to cover non-linear cases, including elasto-plastic deformations in the off-axis ply as well as delamination predictions using a compatible off-axis cohesive element.

CRediT authorship contribution statement

Lars P. Mikkelsen: Conceptualization, Project administration, Writing – original draft, Writing – review & editing, Supervision. **Brian N. Legarth:** Conceptualization, Supervision, Writing – review & editing. **Leon Herrmann:** Data curation, Investigation, Writing – original draft, Writing – review & editing. **Mikkel M. Christensen:** Data curation, Writing – review & editing, Investigation. **Christian F. Niordson:** Conceptualization, Methodology, Supervision, Writing – original draft, Writing – review & editing.

Declaration of competing interest

The authors declare that they have no known competing financial interests or personal relationships that could have appeared to influence the work reported in this paper.

References

[1] Reifsnider KL, Jamison R. Fracture of fatigue-loaded composite laminates. Int J Fatigue 1982;4(4):187–97. http://dx.doi.org/10.1016/0142-1123(82)90001-9.

[2] Tong J, Guild FJ, Ogin SL, Smith PA. On matrix crack growth in quasi-isotropic laminates—I. Experimental investigation. Compos Sci Technol 1997;57(11):1527–35. http://dx.doi.org/10.1016/S0266-3538(97)00080-8.

[3] Talreja R. Fatigue of composite materials: Damage mechanisms and fatigue-life diagrams. Proc R Soc Lond Ser A Math Phys Eng Sci 1981;378(1775):461–75. http://dx.doi.org/10.1098/rspa.1981.0163.

[4] Jamison RD, Schulte K, Reifsnider KL, Stinchcomb WW. Characterization and analysis of damage mechanisms in tension-tension fatigue of graphite/epoxy laminates. Astm Spec Tech Publ 1984;21–55.

[5] Beuth JL. Cracking of thin bonded films in residual tension. Int J Solids Struct 1992;29(13):1657–75. http://dx.doi.org/10.1016/0020-7683(92)90015-L.

[6] Ho S, Suo Z. Tunneling cracks in constrained layers. J Appl Mech 1993;60:890–4. http://dx.doi.org/10.1115/1.2900998.

[7] Hutchinson JW, Suo Z. Mixed mode cracking in layered materials. Adv Appl Mech 1991;29:63–191. http://dx.doi.org/10.1016/S0065-2156(08)70164-9.

[8] Lundmark P, Varna J. Stiffness reduction in laminates at high intralaminar crack density: Effect of crack interaction. Int J Damage Mech 2011;20(2):279–97. http://dx.doi.org/10.1177/1056789509351840.

[9] Carraro PA, Maragoni L, Quaresimin M. Characterisation and analysis of transverse crack-induced delamination in cross-ply composite laminates under fatigue loadings. Int J Fatigue 2019;129(April):105217. http://dx.doi.org/10.1016/j.ijfatigue.2019.105217.

[10] Cox BN, Marshall DB. Crack initiation in fiber-reinforced brittle laminates. J Am Ceram Soc 1996;79(5):1181–8. http://dx.doi.org/10.1111/j.1151-2916.1996.tb08570.x.

[11] Crossman FW, Warren WJ, Wang ASD, Law GE. Initiation and growth of transverse cracks and edge delamination in composite laminates part 2. Experimental correlation. J Compos Mater 1980;14(1):88–108. http://dx.doi.org/10.1177/002199838001400107.

[12] Wang ASD, Crossman FW. Initiation and growth of transverse cracks and edge delamination in composite laminates part 1. An energy method. J Compos Mater 1980;14(1):71–87. http://dx.doi.org/10.1177/002199838001400106.

[13] Quaresimin M, Carraro P, Mikkelsen LP, Lucato N, Vivian L, Brøndsted P, et al. Damage evolution under cyclic multiaxial stress state: A comparative analysis between glass/epoxy laminates and tubes. Compos. B. Eng. 2014;61:282–90. http://dx.doi.org/10.1016/j.compositesb.2014.01.056.

[14] Maragoni L, Carraro PA, Quaresimin M. Periodic boundary conditions for FE analyses of a representative volume element for composite laminates with one cracked ply and delaminations. Compos Struct 201:932–41. http://dx.doi.org/10.1016/j.compstruct.2018.06.058.

[15] Mikkelsen LP, Klitgaard SJ, Niordson CF, Sørensen BF. Tunneling cracks in arbitrary oriented off-axis lamina. Int J Fract 2020;226:161–79. http://dx.doi.org/10.1007/s10704-020-00485-9.

[16] Bangaru AK, Mikkelsen LP, Legarth BN, Sørensen BF. Numerical analysis of tunneling cracks in multidirectional laminates subjected to biaxial loading; scaling down to uniaxial testing. Compos Struct 2021;269:113935. http://dx.doi.org/10.1016/j.compstruct.2021.113935.

[17] Mikkelsen LP, Legarth BN, Herrmann L, Christensen MM, Niordson CF. A special finite element applied to tunnel cracking in laminates [data set]. Zenodo 2021. http://dx.doi.org/10.5281/zenodo.4421512.

[18] Bao G, Ho S, Suo Z, Fan B. The role of material orthotropy in fracture specimens for composites. Int J Solids Struct 1992;29(9):1105–16. http://dx.doi.org/10.1016/0020-7683(92)90138-J.

[19] Suo Z, Bao G, Fan B, Wang TC. Orthotropy rescaling and implications for fracture in composites. Int J Solids Struct 1991;28(2):235–48. http://dx.doi.org/10.1016/0020-7683(91)90208-W.

[20] Mikkelsen LP. Implementing a gradient dependent plasticity model in ABAQUS. In: 2007 abaqus user conference. Paris, France: SIMULIA; 2007, p. 482–92.

[21] Sørensen BF, Jacobsen TK. Characterizing delamination of fibre composites by mixed mode cohesive laws. Compos Sci Technol 2009;69(3–4):445–56. http://dx.doi.org/10.1016/j.compscitech.2008.11.025.

[22] Crossman F, Wang A. The dependence of transverse cracking and delamination on ply thickness in graphite/epoxy laminates. In: Reifsnider K, editor. Damage in composite materials: basic mechanisms, accumulation, tolerance, and characterization. ASTM International; p. 118–22. http://dx.doi.org/10.1520/STP34324S.

[23] Jespersen KM, Mikkelsen LP. Three dimensional fatigue damage evolution in non-crimp glass fibre fabric based composites used for wind turbine blades. Compos Sci Technol 2017;153:261–72. http://dx.doi.org/10.1016/j.compscitech.2017.10.004.

[24] Wang Y, Mikkelsen LP, Pyka G, Withers PJ. Time-lapse helical X-ray computed tomography (CT) study of tensile fatigue damage formation in composites for wind turbine blades. Materials 2018;11:2340. http://dx.doi.org/10.3390/ma11112340.

[25] Vajari DA, González C, Llorca J, Legarth BN. A numerical study of the influence of microvoids in the transverse mechanical response of unidirectional composites. Compos Sci Technol 2014;97:46–54. http://dx.doi.org/10.1016/j.compscitech.2014.04.004.